The Astrophysical Journal, 598:1375–1386, 2003 December 1

OBSERVATIONAL TESTS OF DAMPING BY RESONANT ABSORPTION IN CORONAL LOOP OSCILLATIONS

Markus J. Aschwanden and Richard W. Nightingale
Lockheed Martin Advanced Technology Center, Solar and Astrophysics Laboratory,
Department L9-41, Building 252, 3251 Hanover Street, Palo Alto, CA 94304;
aschwanden@lmsal.com

and

Jesse Andries, Marcel Goossens, and Tom Van Doorsselaere
Centre for Plasma Astrophysics, Katholieke Universiteit Leuven,
Celestijnenlaan 200 B, 3001 Heverlee, Belgium;
jesse.andries@wis.kuleuven.ac.be, marcel.goossens@wis.kuleuven.ac.be,
tomvd@wis.kuleuven.ac.be
Received 2003 June 18; accepted 2003 August 13

ABSTRACT

One of the proposed damping mechanisms of coronal (transverse) loop oscillations in the kink mode is resonant absorption as a result of the Alfvén speed variation at the outer boundary of coronal loops. Analytical expressions for the period and damping time exist for loop models with thin nonuniform boundaries. They predict a linear dependency of the ratio of the damping time to the period on the thickness of the nonuniform boundary layer. Ruderman and Roberts used a sinusoidal variation of the density in the nonuniform boundary layer and obtained the corresponding analytical expression for the damping time. Here we measure the thickness of the nonuniform layer in oscillating loops for 11 events, by forward-fitting of the cross-sectional density profile $n_e(r)$ and line-of-sight integration to the cross-sectional fluxes $F(r)$ observed with *TRACE* 171 Å. This way we model the internal (n_i) and external electron density (n_e) of the coronal plasma in oscillating loops. This allows us to test the theoretically predicted damping rates for thin boundaries as a function of the density ratio $\chi = n_e/n_i$. Since the observations show that the loops have nonuniform density profiles, we also use numerical results for damping rates to determine the value of χ for the loops. We find that the density ratio predicted by the damping time, $\chi_{\rm LEDA} = 0.53 \pm 0.12$, is a factor of ≈1.2–3.5 higher than the density ratio estimated from the background fluxes, $\chi = 0.30 \pm 0.16$. The lower densities modeled from the background fluxes are likely to be a consequence of the neglected hotter plasma that is not detected with the *TRACE* 171 Å filter. Taking these corrections into account, resonant absorption predicts damping times of kink-mode oscillations that are commensurable with the observed ones and provides a new diagnostic of the density contrast of oscillating loops.

Subject headings: Sun: corona — Sun: magnetic fields — Sun: UV radiation — waves

1. INTRODUCTION

Oscillations of coronal loops have now been detected virtually in all wavelengths (for a recent review see, e.g., Aschwanden 2003). Most of these oscillations have been interpreted in terms of standing (eigenmodes) and propagating MHD waves (for a recent theoretical review see, e.g., Roberts & Nakariakov 2003). The MHD eigenmodes include fast sausage and kink modes that produce transverse oscillations with Alfvénic speed, slow magnetoacoustic modes that produce longitudinal oscillations with sound speed, and torsional modes that produce sheared azimuthal oscillations. Obviously, observations of such oscillating systems provide direct measurements of Alfvén speeds and sound speeds, which in combination with electron density measurements can be used to infer the magnetic field in the corona, which is very difficult to determine by other means. This important new diagnostic has been dubbed "coronal seismology" (Roberts, Edwin, & Benz 1984; Roberts & Nakariakov 2003).

Most of the coronal loops that exhibit oscillations have been found to be strongly damped, typically having an exponential damping time t_D of a few oscillation periods P (Nakariakov et al. 1999; Schrijver, Aschwanden, & Title 2002; Aschwanden et al. 2002). Theoretical models of damping mechanisms include (1) nonideal effects such as viscous and ohmic damping, optically thin radiation, and thermal conduction; (2) wave leakage across the sides of the loop boundaries; (3) wave leakage at the chromospheric footpoints; (4) phase mixing in inhomogeneous loop regions; and (5) resonant damping at the sides of loop boundaries. The first three effects are believed to be weak for fast kink-mode oscillations, while the latter two are considered as most important (Goossens 1991; Poedts 2002; Ruderman & Roberts 2002; Ofman & Aschwanden 2002; Goossens, Andries, & Aschwanden 2002; Erdélyi 2003). First observational tests with *TRACE* data revealed that the scaling law of the damping time as a function of other physical parameters (loop length L and period P) favors the phase mixing mechanism (Ofman & Aschwanden 2002), but the mechanism of resonant absorption can explain the observed damping times equally well if the inhomogeneity length scale is a fraction of ≈15%–50% of the loop radius (Goossens et al. 2002). More accurate tests to decide between these two damping mechanisms require the knowledge of the inhomogeneity length scale l and the density ratio n_e/n_i between the external and internal electron density of oscillating loops. The knowledge of the density ratio n_e/n_i

is also required to calculate a coronal magnetic field strength B from a loop with oscillation period P and length L, which is a fundamental tool of coronal seismology (Nakariakov & Ofman 2001). In this paper we measure for the first time these additionally required parameters in 11 kink-mode oscillations events, for which the damping times have been reliably determined earlier (Aschwanden et al. 2002). This allows for a more rigorous quantitative test of the damping mechanisms, with no free parameters for the theoretical model of resonant absorption. We find that the mechanism of resonant absorption is commensurable with the observed damping times. The data analysis and discussion of observational parameters are discussed in § 2, while conclusions are summarized in § 3.

2. DATA ANALYSIS

We analyze 11 loop oscillation events from the study of Aschwanden et al. (2002) for which a reliable damping time t_D has been determined (see, e.g., event 1 in Fig. 1). The same data set of these 11 events is also studied in Ofman & Aschwanden (2002) and Goossens et al. (2002). The date and times of the observations, the heliographic coordinates, the inclination angles of the loop planes, the loop curvature radii, the oscillation periods, and the damping times are summarized in Table 1, extracted from Tables 1 and 2 in Aschwanden et al. (2002), as well as one damping time from Nakariakov et al. (1999).

2.1. *Parameterization of Loop Skin Depth*

Damping of oscillations and waves by resonant absorption has been studied as a mechanism for coronal heating. Most studies in this context are concerned with driven waves. The interest for the present paper is in the eigenmodes damped by resonant absorption. Hollweg & Yang (1988) derived an analytical expression for the decay time in planar geometry for an equilibrium model with a thin nonuniform boundary layer. They translated their Cartesian result to cylindrical flux tubes and were the first to point out that kink-mode oscillations undergo fast damping. In our view "Hollweg decay" is a good name to refer to this fast damping due to resonant absorption. Goossens et al. (1992) derived analytical expressions for the damping rate for one-dimensional cylindrical flux tubes with thin nonuniform boundaries (TB) under rather general conditions of the equilibrium magnetic field and stationary equilibrium velocity field. Of particular relevance for the present study is their

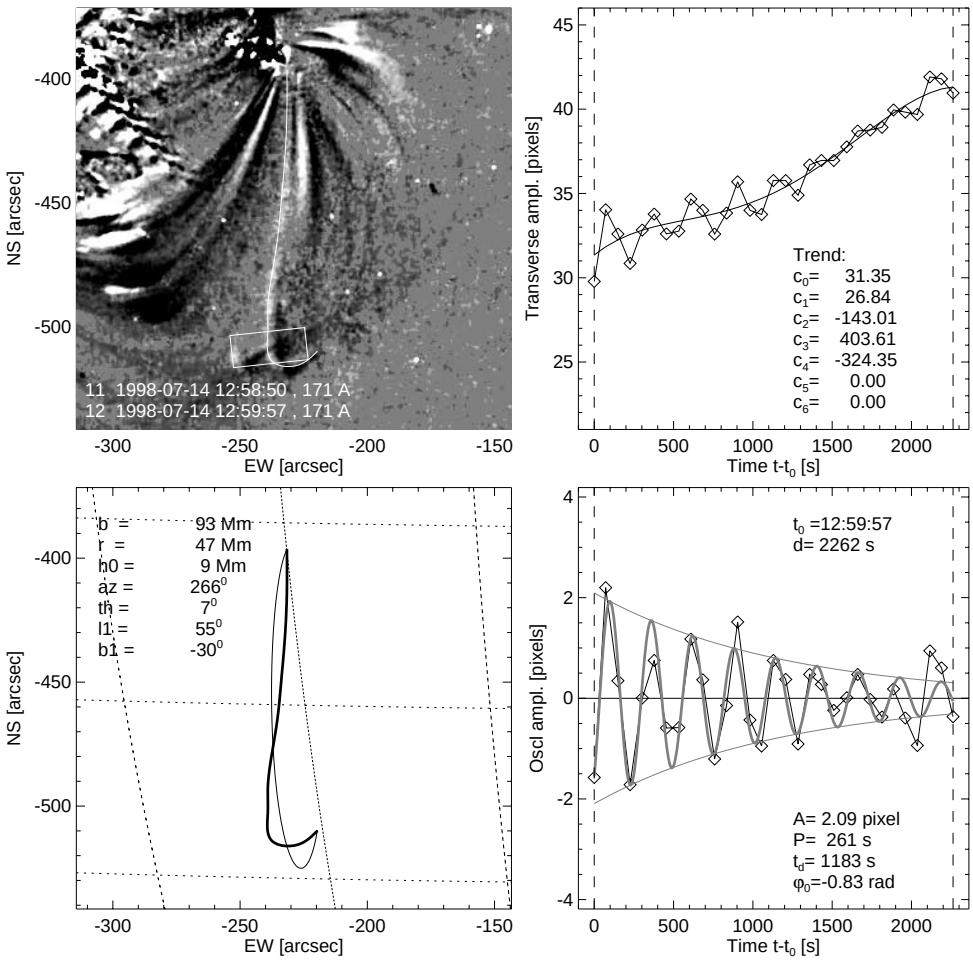

FIG. 1.—Oscillation event 1a on 1998 July 14, 12:45 UT, analyzed in Aschwanden et al. (2002) and Nakariakov et al. (1999). A difference image is shown, where the transverse oscillation amplitude is analyzed in an area marked with a white box that is oriented perpendicular to the loop (*top left-hand panel*). The three-dimensional geometry of the loop is approximated with a coplanar circle (*thin line in bottom left-hand panel*). The oscillation amplitude is decomposed into a nonoscillatory trend (*top right-hand panel*) and into an oscillatory damped function (*bottom right-hand panel*). For further details see Aschwanden et al. (2002).

TABLE 1

TIMES, LOCATIONS, LOOP GEOMETRIES, OSCILLATION PERIODS, AND DAMPING TIMES OF 11 OSCILLATION EVENTS ANALYZED IN ASCHWANDEN ET AL. (2002)

Number	Date and Time of Observation	Heliographic Longitude $l_0 - l_\odot$ (deg)	Heliographic Latitude $b_0 - b_\odot$ (deg)	Loop Inclination ϑ (deg)	Loop Curvature $R_{\rm curv}$ (Mm)	Oscillation Period P (s)	Damping Time t_D (s)
1a	1998 Jul 14 1259:57	−15.6	−27.6	7.0	47.0	261	870[a]
1b	1998 Jul 14 1257:38	−15.5	−26.0	19.0	24.0	265	300
1d	1998 Jul 14 1257:36	−19.5	−24.5	−35.0	55.0	316	500
1f	1998 Jul 14 1256:32	−19.6	−24.5	−44.0	57.0	277	400
1g	1998 Jul 14 1302:26	−19.2	−22.7	47.0	45.0	272	849
3a	1998 Nov 23 0635:57	82.3	−27.7	−12.0	99.0	522	1200
4a	1999 Jul 04 0833:17	26.0	−27.3	−14.0	74.0	435	600
5c	1999 Oct 25 0628:56	−22.9	−21.3	2.0	53.0	143	200
10a	2001 Mar 21 0232:44	72.6	−3.8	20.0	77.0	423	800
16a	2001 May 15 0257:00	22.7	−18.3	39.0	68.0	185	200
17a	2001 Jun 15 0632:29	−48.7	−28.0	41.0	33.0	396	400

[a] This value of $t_D = 870$ s was measured in Nakariakov et al. 1999 and is also used in the study of Ofman & Aschwanden 2002. An alternative value of $t_D = 1200$ s was determined in Aschwanden et al. 2002. The difference reflects a typical uncertainty in the determination of the damping time t_D.

equation (77) for a static loop with a straight field. It was derived under the assumption that the loop is long so that the tube is thin (TT). Ruderman & Roberts (2002) reconsidered the problem as an initial value problem. They arrived at an analytical expression for the damping rate that is a special case of the corresponding equation of Goossens et al. (1992; see their eq. [56]). Ruderman & Roberts (2002) then specialized to a sinusoidal variation of density in the thin nonuniform layer (their eq. [71]) and obtained the corresponding decay time (their eq. [73]). Their density profile $n(r)$ across a loop cross section is parameterized by

$$n(r) = \begin{cases} n_i & \text{for } r < (a-l)\ , \\ n_i \left[\dfrac{(1+\chi)}{2} - \dfrac{(1-\chi)}{2} \right. & \\ \quad \left. \times \sin \dfrac{\pi}{2} \dfrac{(2r+l-2a)}{l} \right] & \text{for } (a-l) < r < a\ , \\ n_e & \text{for } r > a\ , \end{cases} \tag{1}$$

where $\chi = n_e/n_i$ is the density ratio of the external plasma n_e to the internal plasma density n_i of the loop. The depth l of the loop surface region might be called the "skin depth" because it characterizes the depth of the outer envelope layer over which the density varies. Thus, a is the outer loop radius, $b = a - l$ the inner loop radius, and R the mean radius, which defines also the half-width ($w_{\rm loop}/2$) for the loop,

$$R = \frac{w_{\rm loop}}{2} = \left(\frac{a+b}{2} \right) = a - \frac{l}{2}\ . \tag{2}$$

Hence, the density outside of the loop is $n(r > a) = n_e$, the skin region is bound by $b < r < a$, and the density inside this skin depth is $n(r < b) = n_i$. An example of such a density profile is shown in Figure 2 (*bottom panel*), for an inner radius $b = 0.4$ Mm and an outer radius $a = 3.5$ Mm.

With this parameterization, Ruderman & Roberts (2002) derive a ratio of the exponential damping time t_D to the oscillation period P (their eq. [73]), where we can replace

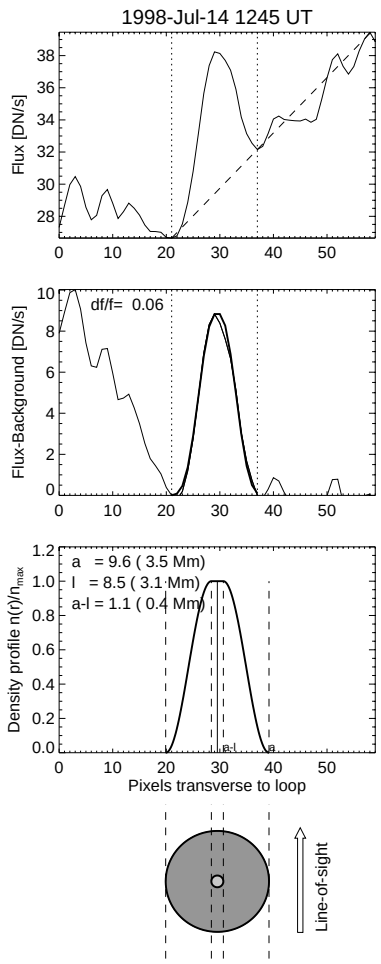

FIG. 2.—Radial flux profile $F(r)$ for event 1a (*top panel*; see Fig. 1), as a function of the cross-sectional radius r perpendicular to the loop and averaged along the loop within the white box shown in the top left-hand panel of Fig. 1. A linear background to the oscillating loop is evaluated (*dashed line in top panel*) and subtracted (*second panel*). A trapezoidal density function with sinusoidal boundaries (eq. [1]) with outer radius a and inner radius $a - l$ is shown (*third panel*) and fitted to the background-subtracted flux cross section (*second panel*) with proper line-of-sight integration across the two-dimensional density distribution (*bottom panel*).

TABLE 2
BEST-FIT PARAMETERS OF LOOP CROSS SECTION FITS TO THE SAME 11 EVENTS SPECIFIED IN TABLE 1

Number	Loop Flux $F_{\rm subtr}$ (DN s^{-1})	Background Flux $F_{\rm back}$ (DN s^{-1})	Loop Radius a (Mm)	Skin Depth l (Mm)	Loop Density $(n_i^2 - n_e^2)^{1/2}$ (10^8 cm^{-3})	Minimum Ratio $(t_D/P)_{\rm min}$	Observed Ratio $(t_D/P)_{\rm obs}$
1a	9.9 ± 1.6	23.2 ± 1.8	3.5 ± 0.4	3.3 ± 0.5	15.6 ± 1.3	0.35 ± 0.53	3.33 ± 1.11
1b	20.9 ± 5.0	28.0 ± 8.1	3.4 ± 0.5	2.9 ± 0.5	22.4 ± 2.7	0.41 ± 0.26	1.13 ± 0.38
1d	4.0 ± 3.1	18.6 ± 7.5	2.6 ± 0.9	2.1 ± 1.1	10.8 ± 4.3	0.48 ± 0.59	1.58 ± 0.53
1f	0.5 ± 0.3	7.3 ± 3.0	2.0 ± 0.5	1.6 ± 0.6	4.5 ± 1.6	0.49 ± 0.42	1.44 ± 0.48
1g	7.0 ± 2.8	43.2 ± 3.7	3.4 ± 0.7	2.9 ± 1.0	12.7 ± 2.8	0.44 ± 0.55	3.12 ± 1.04
3a	12.7 ± 5.3	34.7 ± 1.3	12.4 ± 4.1	10.8 ± 4.3	9.1 ± 2.0	0.41 ± 0.40	2.30 ± 0.77
4a	12.6 ± 2.2	54.4 ± 12.6	2.8 ± 0.5	2.7 ± 0.5	19.8 ± 1.7	0.34 ± 0.38	1.38 ± 0.46
5c	13.9 ± 2.9	44.8 ± 6.3	2.5 ± 0.2	2.3 ± 0.2	21.9 ± 2.3	0.37 ± 0.26	1.40 ± 0.47
10a	25.9 ± 8.4	40.5 ± 6.5	4.6 ± 0.5	3.6 ± 0.8	20.7 ± 3.4	0.48 ± 0.36	1.89 ± 0.63
16a	2.5 ± 0.5	6.3 ± 1.5	10.2 ± 2.9	9.0 ± 3.3	4.4 ± 0.4	0.40 ± 0.59	1.08 ± 0.36
17a	1.2 ± 0.7	53.6 ± 2.0	1.6 ± 0.6	1.2 ± 0.7	7.1 ± 2.9	0.57 ± 0.40	1.01 ± 0.34

$R \approx a$ in the thin-boundary approximation,

$$\left(\frac{t_D}{P}\right)_{\rm thin} = \frac{2}{\pi}\left(\frac{a}{l}\right)\frac{(1+\chi)}{(1-\chi)} \approx \frac{2}{\pi}\left(\frac{R}{l}\right)\frac{(1+\chi)}{(1-\chi)} \ . \quad (3)$$

Ruderman & Roberts (2002) obtained the above analytical expression (and also their more general expression, eq. [56]) under the assumption that the nonuniform layer is thin, meaning $l/a \ll 1$. In the present paper we use the Ruderman & Roberts (2002) formula to estimate the ratio χ for loops with thick nonuniform layers. A generalization of this result for thick boundary layers thus involves two corrections, one for the replacement of the outer loop radius a with the mean loop radius $R = a - l/2$, and a second one that quantifies a correction factor $q_{\rm TB}$ between the thick-boundary and thin-boundary treatment using the mean loop radius R. Thus, the damping formula may be written in terms of R and the correction factor $q_{\rm TB}$,

$$\left(\frac{t_D}{P}\right)_{\rm thick} = q_{\rm TB}\left(\frac{t_D}{P}\right)_{\rm thin} = q_{\rm TB}\left(\frac{2}{\pi}\frac{R}{l}\right)\frac{(1+\chi)}{(1-\chi)} \ , \quad (4)$$

where the correction factor $q_{\rm TB}$ depends on the boundary thickness ratio (l/R), as well as on the density ratio χ, and has been calculated numerically in T. Van Doorsselaere et al. (2003, in preparation). For instance, for a density ratio of $\chi = \frac{1}{3}$, the correction factor $q_{\rm TB}$ varies in the range of [0.75, 1.18]. In the fully nonuniform limit $l/R = 2$, the correction value is $q_{\rm TB}(l/R = 2,\ \chi = \frac{1}{3}) \approx 0.75$. We use the numerically calculated values $q_{\rm TB}$ in Table 2 to predict the external plasma density.

In a previous study we measured the oscillation periods P and damping times t_D of 11 events (Aschwanden et al. 2002). Here we attempt to measure the loop geometry parameters a and $b = a - l$ and the density ratio χ to test this theoretical model (eq. [4]) of damping by resonant absorption. The "density contrast" of the oscillating loop is just the inverse ratio $\chi^{-1} = n_i/n_e$, which is larger than unity for every detectable loop.

2.2. *Loop Density Profiles*

In order to measure cross-sectional density profiles $n(r)$ of coronal loops observed in optically thin EUV or soft X-ray emission, at least four effects that need to be taken into account play a role: the subtraction of the background flux from the plasma in front and behind the oscillating loop along the line of sight (Fig. 2), the line-of-sight integration of the emission measure (Fig. 3), the spatial smearing due to the transverse motion of an oscillating loop during an exposure time (Fig. 4), and the point-spread function of the instrument (Fig. 5).

We start with the background subtraction, which is simply done by inspecting cross-sectional density profiles, averaged over some loop segment along the loop, selecting the lowest flux values on both sides of the oscillating loop, and interpolating a linear function between both sides (Fig. 2, *top panel*). Thus, the total EUV flux per pixel across a loop cross section is defined by

$$F(r,t) = F_{\rm back}(r,t) + F_{\rm loop}(r,t) \ , \quad (5)$$

which yields a time-averaged background flux $F_{\rm back}$ (per pixel),

$$F_{\rm back} = \langle F_{\rm back}(r,t)\rangle \ , \quad r_{\rm left}(t) < r < r_{\rm right}(t) \ , \quad (6)$$

and a time-averaged loop flux $F_{\rm loop}$ at the central axis of the

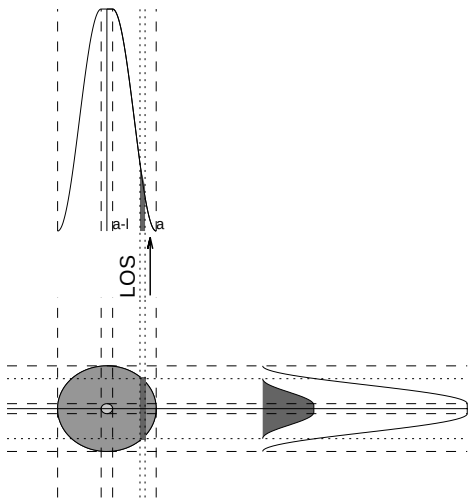

FIG. 3.—Geometry of line-of-sight (LOS) integration. The two-dimensional density distribution of a loop cross section is contoured in gray scale in the bottom left part, cross sections along the line of sight are projected to the right side, and the radial cross section in transverse direction (in the plane of the sky) is projected to the top side.

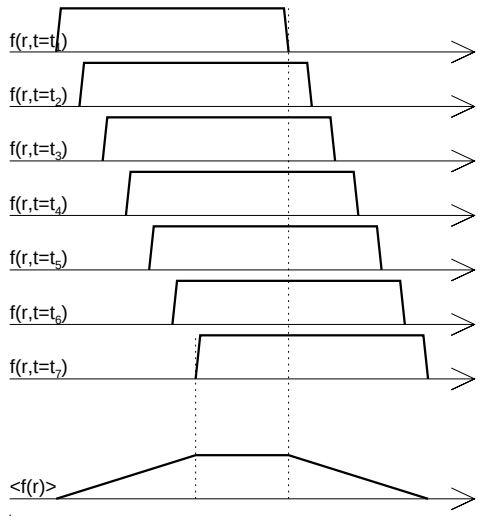

FIG. 4.—Effect of time smearing demonstrated for a near-rectangular cross section profile $F(t, t = t_i)$, $i = 1, \ldots, 7$, which in superposition adds up to a more trapezoidal cross section profile $\langle F(r) \rangle$.

loop,

$$F_{\rm loop} = \max\left[F_{\rm loop}(r,t)\right] , \quad r_{\rm left}(t) < r < r_{\rm right}(t) , \quad (7)$$

where the loop boundaries $[r_{\rm left}(t), r_{\rm right}(t)]$ vary as a function of time t depending on the motion of the oscillating loop (see Fig. 6, *left-hand panel*). The loop flux is related to the electron density $n(z)$ along the line of sight z by the emission measure EM at pixel position (x, y),

$$\frac{d{\rm EM}(x,y,T)}{dT} = \int n^2(x,y,z,T)dz . \quad (8)$$

The observed flux $F_{\rm loop}(x, y)$ in a given filter specified by a temperature-dependent instrumental response function $R(T)$ is obtained by integrating the emission measure ${\rm EM}(T)$ with the response function $R(T)$ over all temperatures T,

$$F_{\rm loop}(x,y) = \int \frac{d{\rm EM}(x,y,T)}{dT} R(T)dT . \quad (9)$$

For an isothermal loop segment that is near-perpendicular to the line of sight, we can obtain the radial flux profile $F(r)$ by integrating the density profile $n(r)$ specified in equation

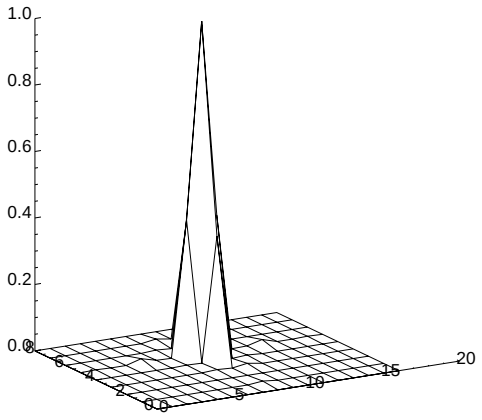

FIG. 5.—Point-spread function of the *TRACE* 171 Å filter measured by a BID algorithm. The mesh corresponds to CCD pixels with a pixel size of $0''.5$ (courtesy of R. Nightingale).

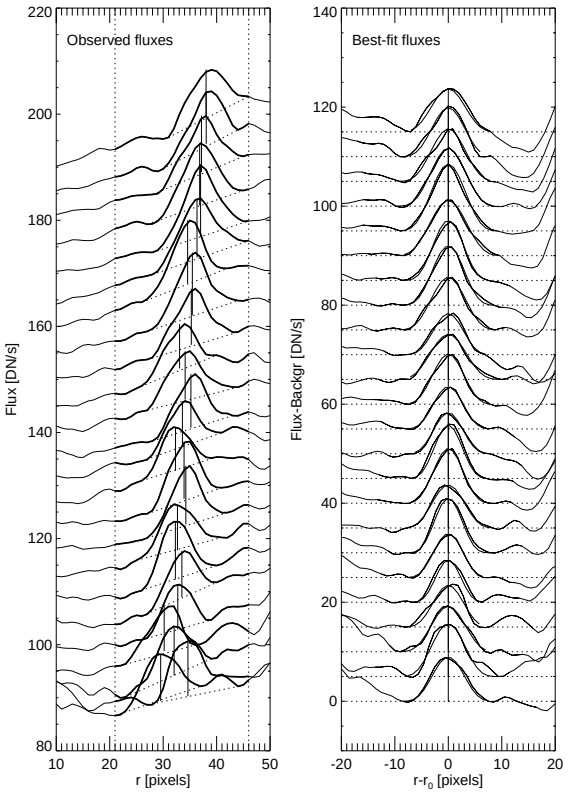

FIG. 6.—Cross-sectional fluxes $F(r, t_i)$ for event 1a shown for time steps $i = 1, \ldots, 24$ (*left-hand panel*), averaged within the white box area indicated in the top left-hand panel of Fig. 1. The flux profiles are incrementally shifted by 5 flux units for clarity. The background fluxes are indicated with dotted lines, the loop center location r_0 with a vertical solid line. The best-fit flux profiles $F(r - r_0, t_i)$ are shown in the right-hand panel (*thick lines*), based on the density profile $n_e(r)$ (eq. [1]) obtained by forward-fitting of the line-of-sight integration and instrumental response function. Note that the cross-sectional flux profile is almost invariant during this entire time interval of the observed observation.

(1) along the line of sight z (Fig. 2, *bottom panel*, and Fig. 3),

$$F_{\rm loop}(r) = R(T) \int n^2\left(r' = \sqrt{r^2 + z^2}\right)dz . \quad (10)$$

The circular cross section essentially causes a convolution of the density profile $n(r)$ with a column depth Δz that has a circular dependence $\Delta z \propto [(a^2 - r^2)]^{1/2}$, so that the flux profile $F(r)$ looks more Gaussian-like (Fig. 2, *second panel*) than the trapezoidal shape of the density function (Fig. 2, *third panel*). We fit the (normalized) theoretical loop profile (eq. [1]) to the observed flux profiles $F_{\rm loop}(r)$ by optimization of the parameters a and l, using a Powell minimization method (Press et al. 1986).

The measured total flux at the center ($r = 0$) of the loop is

$$F_{\rm total} = \left[n_i^2 w_{\rm loop} + n_e^2\left(z_{\rm back} - w_{\rm loop}\right)\right]R(T) , \quad (11)$$

with n_i being the internal loop density, $w_{\rm loop}$ the mean loop width (eq. [2]), and n_e the external or average background density extended over a column depth $z_{\rm back}$. The mean background flux measured at the sides of the loop is

$$F_{\rm back} = (n_e^2 z_{\rm back})R(T) , \quad (12)$$

yielding a background-subtracted flux of

$$F_{\rm subtr} = F_{\rm total} - F_{\rm back} = \left[\left(n_i^2 - n_e^2\right)w_{\rm loop}\right]R(T) , \quad (13)$$

which then yields the difference of the squared densities. Thus, we cannot determine the internal loop density n_i directly, but only as a function of the external density n_e,

$$n_i = \sqrt{\frac{\Delta F_{\rm subtr}}{w_{\rm loop} R(T)} + n_e^2}\ . \qquad (14)$$

In the limit of vanishing (background-subtracted) loop flux, $F_{\rm subtr} \mapsto 0$, the densities inside (n_i) and outside of the loop (n_e) become identical. The density profile fitting is performed for every time step (typically 10–30 images) of the 11 oscillation events (see, e.g., Fig. 6). The results of the best-fit parameters a, l, and $(n_i^2 - n_e^2)^{1/2}$, with the mean and standard deviation from averaging over all (≈20–30) time steps, are given in Table 2.

The data analysis procedure is illustrated in Figures 1–8. Figure 2 shows a fit of a cross section profile $n(r, t_i)$ to the observed flux $F_{\rm loop}(r, t = t_i)$ at a single time step t_i. Figure 6 shows the fits as a function of time t_i, $i = 1, \ldots, n$, and Figure 7 shows the variation of the measured parameters as a function of time, $F_{\rm loop}(t)$ and $F_{\rm back}(t)$ (Fig. 7, *top panel*), the oscillation amplitude $A(t)$ (Fig. 7, *middle panel*), and the cross section parameters $a(t)$, $l(t)$, and $a(t) - l(t)$ (Fig. 7, *bottom panel*), with the means and standard deviations indicated. Figure 8 shows a summary plot of the average cross section fits, for each of the 11 events.

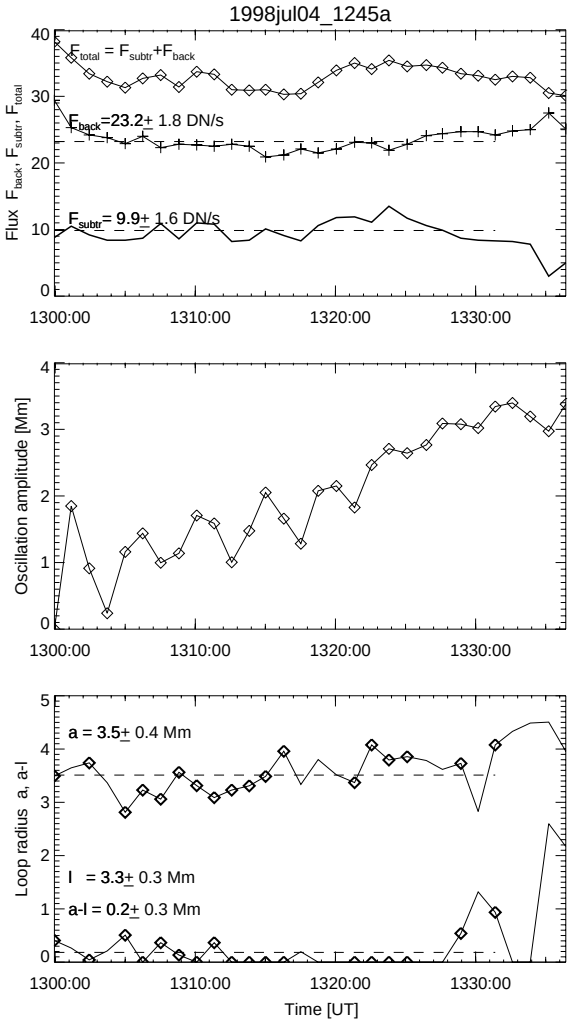

FIG. 7.—Physical parameters of the best-fit cross section profiles as a function of time for event 1a: total flux $F_{\rm total}(t) = F_{\rm back}(t) + F_{\rm loop}(t)$, background flux $F_{\rm back}(t)$, and loop flux $F_{\rm loop}(t)$ (*top panel*); oscillation amplitude $A(t)$ (*middle panel*); and density profile parameters $a(t)$ and $l(t)$ (eq. [1]) (*bottom panel*). Acceptable fits (with deviations of $df/f < 10\%$ in the flux profile) are marked with diamonds.

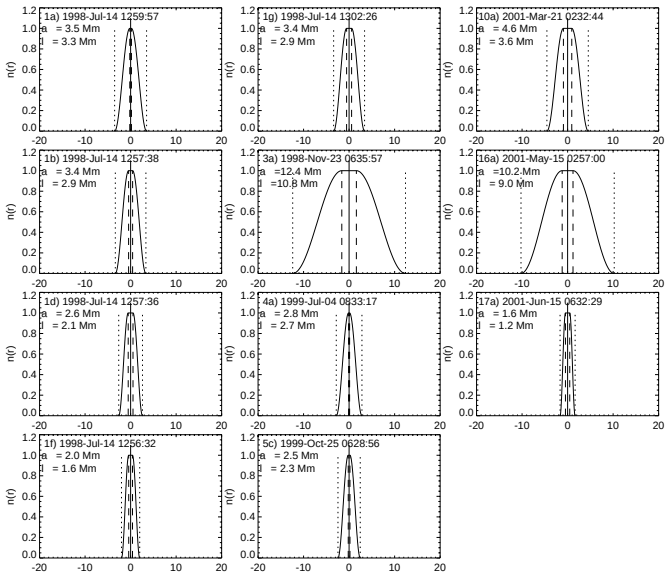

FIG. 8.—Best-fit density profiles $n_e(r)$ as a function of radial distance from loop center r (Mm) for all 11 events. The dates of the events and the best-fit parameters a and l are indicated in each panel. Each profile is averaged over 10–30 time steps during the time interval of the observed loop oscillation.

2.3. *Oscillatory Motion Smearing*

We have to be aware that every *TRACE* image has been recorded with a finite exposure time of typically $\Delta t_{\rm exp} \approx 5$–10 s. Since we are measuring the loop profiles in perpendicular direction to the loop axis, the oscillatory motion of the transverse kink mode introduces a smearing that transforms a rectangular density profile into a trapezoidal profile (Fig. 4), if not corrected. For typical oscillation speeds of $v_{\rm max} \approx 10$–100 km s^{-1} (see Table 2 in Aschwanden et al. 2002) we expect a motion of $\Delta r = v_{\rm max} \Delta t_{\rm exp} \approx 50$–1000 km, which corresponds to $\Delta r \approx 0.1$–2.8 *TRACE* pixels with a pixel size of 0.″5. However, the observed loop radii were found to be in the range of $a \approx 2000$–12,000 km, hence at least an order of magnitude larger. For most times the actual speed is smaller at an arbitrary phase of the sinusoidal oscillations, $v(t) < v_{\rm max}$. We measured the actual amount of smearing for every fit and found that it amounted indeed in all cases to a fraction of less than 0.05–0.1 of the loop width. Therefore, we neglected this effect in the fitting procedure.

2.4. *Point-Spread Function*

The instrumental point-spread function contributes to some broadening and smoothing of observed density profiles and thus could affect our inversion of loop density profiles from observed flux profiles. The point-spread function of *TRACE* has been investigated in 171 Å EUV image fits using a blind iterative deconvolution (BID) procedure (R. Nightingale 2003, private communication). The shape

of the *TRACE* point-spread function was found to have the shape of a four-sided pyramid with a square-shaped base rotated by 45° with respect to the CCD raster (Fig. 5). The point-spread function falls off from a central pixel with value 1.0 to 0.33–0.36 in the next-neighbor pixels and almost to 0.0 in the second-next–neighbor pixels, for a pixel size of 0.″5. Thus, the average full width of the pyramid shape is FWHM $= 2 \times 0.''5(1 - 0.345)/0.5 = 1.''3$.

Independently, the *TRACE* point-spread function has also been characterized with a BID procedure by Golub et al. (1999), who also found a slightly elongated shape at a position angle of 45°, with an FWHM of 3 pixels in one direction and 2 pixels in the orthogonal direction, yielding FWHM $= 2.5 \times 0.''5 = 1.''25$, which is consistent with the former measurement.

Since our measured loop widths ($w = 2a - l \approx 2 \ldots 14$ Mm; see Table 1) are on average at least an order of magnitude larger than the FWHM of the point-spread function (FWHM $\approx 1.3 \times 0.725 = 0.94$ Mm), we neglect it in fitting of the density profiles to the flux profiles.

2.5. *Predicted External Plasma Density*

After we have measured the loop profile parameters a and l (§ 2.1 and Table 2), and using the measurements of the observed loop oscillation periods P and damping times t_D from the previous study (Aschwanden et al. 2002), we have only one free parameter left in the damping time expression (eq. [4]), namely, the external-to-internal density ratio $\chi = n_e/n_i$ of the oscillating loop. Because it is difficult to measure the ambient plasma density n_e of an oscillating loop, we do not explicitly predict the damping time ratio t_D/P based on uncertain densities n_e with equation (12), but rather do it the other way around by using the theoretical relation given by equation (12) to predict the ambient density n_e, which can then be compared with observational measurements.

As equation (4) shows, the shortest damping time ratios occur for a loop in vacuum, i.e., for $\chi = 0$. We list these minimum ratios

$$\left(\frac{t_D}{P}\right)_{\rm min} = q_{\rm TB}\left(\frac{2}{\pi}\frac{R}{l}\right) \tag{15}$$

in Table 2, which are calculated from the measured values of $R = a - l/2$ and l and using the fully nonuniform approximation $q_{\rm TB}(l/R \approx 2) \approx 1.0$ (T. Van Doorsselaere et al. 2003, in preparation). The resulting values of $(t_D/P)_{\rm min}$ (Table 2; seventh column) reveal that they are all lower than the observed values (Table 2; rightmost column), as expected for $\chi > 0$. This is a first successful test of the theoretical model, in the sense that all 11 observed cases are able to provide a physical solution, namely, a positive value for the density contrast, $\chi > 0$.

In a next step we express the density contrast χ_D explicitly as a function of the other variables from equation (4) (where the subscript in χ_D indicates here that it is derived from the damping time t_D, instead of the standard definition in terms of density contrast, $\chi = n_e/n_i$, as defined in eq. [1]),

$$\chi_D = \frac{(X-1)}{(X+1)}\ , \quad X = \frac{1}{q_{\rm TB}}\frac{\pi}{2}\left(\frac{l}{R}\right)\left(\frac{t_D}{P}\right)\ . \tag{16}$$

We predict now the density contrasts χ_D based on the measured ratios of damping times t_D to periods P [$(t_D/P)_{\rm obs}$ in Table 2], using the fully nonuniform limit [$q_{\rm TB}(l/R = 2) = 1.0$]. We find values in the range of $\chi_D \approx 0.3$–0.8 (Table 3, eighth column). Using the numerically calculated correction factors $q_{\rm TB}(l/R)$ computed with the LEDA code (T. Van Doorsselaere et al. 2003, in preparation) for the actual observed values of (l/R), indicated with $\chi_{\rm LEDA}$ in Table 3, we see that the approximation $q_{\rm TB} \approx 1.0$ is a very good approximation for fully nonuniform loops ($l/R = 2$).

2.6. *Measurement of the External Plasma Density*

In a next step in our analysis we attempt to estimate the external plasma density n_e around the oscillating loops from the measured background flux $F_{\rm back}$ and loop position. The flux of the background is composed of the emission measure along the line of sight in front and behind the oscillating loop. We assume a stratified atmosphere for the spatial and temporal average of the background flux, with an exponential density scale height λ_T corresponding to a mean temperature T. For the plasma detected in the *TRACE* 171 Å passband, this mean temperature is $T \approx 1.0$ MK. Thus, the vertical density profile of the detected coronal plasma is

$$n_e(h) = n_0 \exp\left(-\frac{h}{\lambda_T}\right)\ , \qquad \lambda_T = 47\ {\rm Mm}\left(\frac{T}{1.0\ {\rm MK}}\right)\ . \tag{17}$$

We need to calculate the column depth of a hydrostatically stratified atmosphere along a line of sight as a function of the distance d from Sun center. We define an "equivalent column depth," $z_{\rm eq}(d, T)$, as a function of the distance $d = r_\odot + h$ from Sun center, for a mean coronal temperature T,

$${\rm EM}_{\rm back}(d, T) = \int_{-\infty}^{\infty} n_e^2[h(z), T]dz = n_0^2(T) z_{\rm eq}(d, T)\ , \tag{18}$$

with $n_0(T)$ the coronal base density as defined in equation (6). From equations (6) and (7), the following relation follows for this equivalent column depth (Table 3, fourth column):

$$z_{\rm eq}(d, T) = \int_{z_1}^{z_2} \exp\left[-\frac{2\left(\sqrt{d^2 + z^2} - r_\odot\right)}{\lambda_T}\right] dz \quad \text{for } d \geq r_\odot\ , \tag{19}$$

with the integration limits $z_1 = -\infty$ and $z_2 = +\infty$ for above-the-limb locations ($d \geq r_\odot$). Inside the disk ($d \leq r_\odot$), we have only to change the integration limit z_2 to

$$z_2(d) = -\sqrt{r_\odot^2 - d^2} \quad \text{for } 0 < d < r_\odot\ . \tag{20}$$

The column depths $z_{\rm eq}(d, T)$ are shown in Aschwanden & Acton (2001; Fig. 3 therein) for a height range from disk center ($d = 0$) to one solar radius outside the limb ($d = 2r_\odot$), for temperatures in the range of $T = 1.0$–4.0 MK. At disk center ($d = 0$), the equivalent column depth matches the emission measure scale height, which is the half-density scale height ($\lambda_{\rm EM} = \lambda_T/2$). At the limb ($d = r_\odot$), there is, in principle, a discontinuous change by a factor of 2, which, however, is difficult to measure because of the extremely high instrumental resolution required to

TABLE 3

MODEL PARAMETERS OF EXTERNAL BACKGROUND PLASMA DENSITY AND DENSITY CONTRAST

Number	Loop Apex Altitude h_{osc} (Mm)	Distance from Center $d_{osc}/r_{\odot}$	Equivalent Column Depth $z_{eq}/r_{\odot}$	External Density n_e (10^8 cm^{-3})	Internal Density n_i (10^8 cm^{-3})	Density Ratio χ	Predicted Ratio χ_D	Numerical Ratio χ_{LEDA}	Density Ratio χ_{LEDA}/χ
1a	46.6	0.561	0.040	3.2 ± 0.3	15.9 ± 1.3	0.20 ± 0.02	0.81 ± 0.27	0.70	3.5
1b	22.7	0.521	0.039	6.0 ± 0.7	23.2 ± 2.7	0.26 ± 0.04	0.46 ± 0.28	0.43	1.6
1d	45.1	0.553	0.040	3.0 ± 1.1	11.2 ± 4.3	0.27 ± 0.14	0.53 ± 0.46	0.52	2.0
1f	41.0	0.551	0.040	2.1 ± 0.7	4.9 ± 1.6	0.42 ± 0.19	0.50 ± 0.35	0.49	1.2
1g	30.7	0.518	0.039	6.3 ± 1.3	14.2 ± 2.8	0.44 ± 0.13	0.75 ± 0.28	0.70	1.6
3a	96.8	1.137	0.008	3.1 ± 0.6	9.6 ± 2.0	0.32 ± 0.09	0.70 ± 0.26	0.64	2.0
4a	71.8	0.675	0.044	2.7 ± 0.2	20.0 ± 1.7	0.14 ± 0.02	0.60 ± 0.37	0.47	3.4
5c	53.0	0.559	0.040	3.9 ± 0.4	22.3 ± 2.3	0.18 ± 0.03	0.58 ± 0.25	0.50	2.8
10a	72.4	1.054	0.109	1.5 ± 0.2	20.8 ± 3.4	0.07 ± 0.02	0.60 ± 0.27	0.58	8.1
16a	52.8	0.524	0.039	1.5 ± 0.1	4.7 ± 0.4	0.32 ± 0.04	0.46 ± 0.60	0.41	1.3
17a	24.9	0.860	0.061	6.3 ± 1.9	9.5 ± 2.9	0.66 ± 0.28	0.28 ± 0.36	0.36	0.5

resolve this jump. Above the limb, the column depth drops quickly with height.

We can now relate the observed background flux $F_{\rm back}(d)$, measured at a line of sight with distance d from disk center, to the emission measure $\mathrm{EM}_{\rm back}(d)$, using the instrumental response function $R(T)$,

$$F_{\rm back}(d) = \mathrm{EM}_{\rm back}(d) R(T) \ , \tag{21}$$

and determine the coronal base density n_0 (with eqs. [9] and [10]),

$$n_0 = \sqrt{\frac{F_{\rm back}(d)}{R(T) z_{\rm eq}(d,T)}} \ . \tag{22}$$

To estimate the ambient density around the oscillating loop in height $h_{\rm osc}$, we have to use the hydrostatic model of equation (6),

$$n_e(h = h_{\rm osc}) = n_0 \exp\left(-\frac{h_{\rm osc}}{\lambda_T}\right) \ . \tag{23}$$

Obviously we need measurements of the center-limb distance d of the location of the oscillating loop segment, as well as an estimate of the altitude $h_{\rm osc}$ of the oscillating loop segment. In the previous study (Aschwanden et al. 2002) we measured the heliographic longitude difference $(l_1 - l_0)$ and latitude difference $(b_1 - b_0)$ of the midpoint of the loop baseline to disk center, the inclination angle ϑ of the loop plane, and the loop curvature radius $R_{\rm curv}$. We list these parameters of our 11 analyzed loops in Table 1. With these geometrical parameters we can now determine the projected distance d of the location of the oscillating loop segment to disk center (Table 3, third column),

$$d = (r_\odot + h_{\rm osc}) \sin\left[(l_1 - l_0)^2 + (b_1 - b_0)^2\right] \ , \tag{24}$$

and the height $h_{\rm osc}$ of the oscillating loop segment above the solar surface (Table 3, second column),

$$h_{\rm osc} = R_{\rm curv} \cos\vartheta \ . \tag{25}$$

Inserting these parameters d and $h_{\rm osc}$ into equations (6)–(12), we obtain now an estimate of the ambient density at the height of the oscillating loops, $n_e(h = h_{\rm osc})$. The so-evaluated density values n_e are given in Table 3 (fifth column), along with the inferred internal densities n_i (eq. [14]) and density ratios $\chi = n_e/n_i$. These density ratios can now be compared with the predicted density contrast χ_D (eq. [5]) from the observed damping times (Table 3). The uncertainties of the derived parameters were estimated according to the error propagation law (see the Appendix). We find that the density ratio is consistent with the model of resonant absorption within a factor of $\chi_{\rm LEDA}/\chi \approx 1.2$–$3.5$ (Table 3, rightmost column, excluding the lowest and highest extreme value).

2.7. *Temperature Corrections*

In our analysis we used the temperature of $T = 1.0$ MK that corresponds to the peak of the *TRACE* 171 Å passband, in which all the analyzed oscillating loops were detected. This peak temperature is certainly representative for the background plasma along the line of sight because it represents an average over many coronal structures that are detected in a given passband with the highest probability near the peak temperature of the temperature sensitivity. Thus, the temperature should not affect any derived parameter based on the background plasma, such as the external plasma density n_e.

What about the temperature inside the oscillating loops? Since the FWHM of the temperature response function in 171 Å is about $\Delta T_{171}/T_{171} = (1.2 - 0.8)/1.0 = 0.4$, a loop is detected with a probability of 67% in this temperature range. The peak response function we used is $R_{171}(T = 1.0\ \mathrm{MK}) = 1.1 \times 10^{-26}$ DN s^{-1} cm^5 (see, e.g., Fig. 12 in Aschwanden et al. 2000). If we approximate the response function with a Gaussian curve, single-temperature plasma structures are detected with a probability of 24% at a sensitivity that is less than 50% of the peak response. Hence, statistically, in every fourth loop we may have overestimated the response function by a factor of $\gtrsim 2$, which is equivalent to an underestimation of the true loop density by a factor of $\lesssim \sqrt{2}$. Therefore, the resulting density contrast $\chi = n_e/n_i$ could be a factor of 1.4 higher for every fourth loop. In the statistical average, however, this temperature correction is not sufficient to explain the average discrepancy between the density ratios, i.e., $\chi_{\rm LEDA}/\chi \approx 1.2$–$3.5$.

2.8. *Coronal Filling Factors*

Another not considered effect is the spatial filling factor, which affects the plasma determination both external and internal to the oscillating loops. Generally, if the filling factor is less than unity, density derivations from the emission measure (eqs. [8], [11], and [19]) result in an underestimate of the density. If both the internal plasma and external plasma are subject to the same filling factor, this effect would cancel out in the density contrast $\chi = n_e/n_i$ and no correction is needed. However, we think that the oscillating flux tubes, especially those with small diameters, are more likely to be solidly filled with plasma than the wide bundles of flux tubes or the background corona. Examining the diameters of the oscillating loops, we find large radii $a \gtrsim 10$ Mm only for two cases (3a and 16a in Table 2), which show the same discrepancy between χ and χ_D as the other cases (Table 3), so a correction by a filling factor of loops cannot improve the consistency between data and model either.

On the other side, we can ask whether the filling factor of the background corona has an effect on our model. With our stratified coronal model we applied for the temporal and spatial average (eq. [6]), we inferred a density contrast of $\chi = 0.30 \pm 0.16$. If the background corona is subject to a filling factor less than unity, the true ambient density around a loop could be lower or higher. A possible bias toward a higher value could result in active regions, where high-density concentrations are more likely around oscillating loops. If we consider such a filling factor bias and assume that the ambient density around an oscillating loop in an active region is actually higher, the density contrast value $\chi = n_e/n_i$ increases. The mismatch is in the average $\chi_{\rm LEDA}/\chi \approx 1.2$–$3.5$, which could be reconciled with correspondingly higher ambient densities around the oscillating loops. This higher density does not necessarily need to be plasma with a temperature of $T \approx 0.8$–1.2 MK as detected with *TRACE* 171 Å; rather, it could be plasma of higher temperature, say, in the range of $T \approx 1.2$–2.0 MK, as many differential emission measure distributions inferred in active regions suggest (e.g., Brosius et al. 1996; Aschwanden &

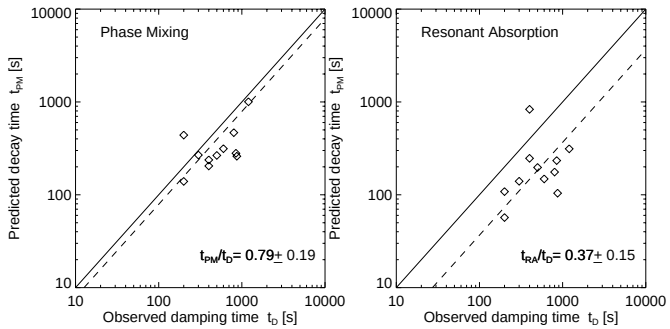

FIG. 9.—*Left*: Scaling of loop oscillation damping time t_D with (aP), which does not show a close correlation. For damping by phase mixing a scaling of $t_D \propto (Pl)^{2/3}$ is expected. *Right*: Scaling of loop oscillation damping time t_D with $(R/l)P$, for which a linear correlation is expected in the framework of resonant absorption. The linear regression fit shows a slope of 0.84 ± 0.34, which is consistent with the expected proportionality.

Acton 2001). Improvements in the determination of the mean external density n_e therefore require the knowledge of the differential emission measure function, which demands multifilter data.

2.9. *Comparison with Phase Mixing Model*

The theory for damping due to resonant absorption for thin nonuniform layers predicts that the damping time t_D is a function of the period P, the geometric ratio (R/l), and the external/internal density ratio $\chi = n_e/n_i$ (eq. [4]), without any free parameter,

$$t_D^{\rm RA} = \frac{2q_{\rm TB}RP}{\pi l}\,\frac{(1+\chi)}{(1-\chi)}\ . \qquad (26)$$

We test this scaling law in Figure 9 (*right panel*) and find a mean ratio of $t_D^{\rm RA}/t_D^{\rm obs} = 0.37 \pm 0.15$, so theory and observations agree within a factor of 3, where the discrepancy probably is due to the underestimation of the background density when measured with a narrowband filter.

Alternatively, we might test the scaling law for phase mixing (Heyvaerts & Priest 1983; Roberts 2000), which predicts the following dependence:

$$t_D^{\rm PM} = \left(\frac{6L^2 l_{\rm inh}^2}{\nu\pi^2 v_{\rm A}^2}\right)^{1/3} = \left(\frac{3}{\nu\pi^2}\right)^{1/3}(Pl)^{2/3}\ , \qquad (27)$$

where L is the loop length, $l_{\rm inh}$ is the scale of inhomogeneity (which we set equal to our skin depth here), ν is the coronal viscosity, and $v_{\rm A}$ is the Alfvén speed inside the flux tube, which amounts to $v_{\rm A} = \sqrt{2}L/P$ for the kink mode in a low-β plasma (Nakariakov & Ofman 2001). We calculate the predicted damping times with a standard value of the coronal viscosity, $\nu = 4 \times 10^{13}$ cm^2 s^{-1}, and plot them in Figure 9 (*left panel*). We find an average ratio of $t_D^{\rm PM}/t_D^{\rm obs} = 0.79 \pm 0.19$, which closely agrees with the observations. Thus, the model of phase mixing cannot be excluded as an alternative interpretation.

A corresponding test of the scaling law $t_D \propto P$ for resonant absorption and $t_D \propto (LP)^{2/3}$ has been performed in Ofman & Aschwanden (2002) that showed also a slight preference for phase mixing. The test here, however, is more constrained. There are three differences to the former study: (1) we do not make the assumption that the spatial scale of inhomogeneity $l_{\rm inh}$ is proportional to the loop length L or loop width w, (2) the loop widths $w_{\rm loop} = a + b$ are measured here from the deconvolved density profiles and not from the FWHM of the flux profiles, and (3) we measure here the (outer) loop radius a and spatial scale of inhomogeneity l separately, which were set equal to each other in the former study. Nevertheless, we obtain similar results that both models are roughly consistent with the observations.

3. CONCLUSIONS

In this study we modeled the cross-sectional density profiles $n_e(r)$ of oscillating loops, specified by the outer radius a, skin depth l, internal density n_i, and external density n_e. These parameters allow us to test the theoretically predicted relation between the damping time t_D, oscillation period P, geometry (a, l), and density parameters (n_e, n_i) for the damping mechanism of resonant absorption. Because we can measure all these observables, we have no free parameters in the model and thus are able to perform a very strict consistency test between theory and observations. The alternative damping mechanism of phase mixing can be tested with these measured parameters also, but there is a free parameter, namely, the viscosity, which cannot directly be constrained by observations to date. Our observational test yields the following results:

1. The means and standard deviations of our measured parameters are as follows (see Table 4): outer loop radius $a = 4.5 \pm 3.5$ Mm, loop skin depth $l = 3.9 \pm 3.1$ Mm, skin depth ratio $l/a = 0.85 \pm 0.08$, internal loop density $n_i = (1.4 \pm 0.7) \times 10^9$ cm^{-3}, external loop density $n_e = (0.36 \pm 0.18) \times 10^9$ cm^{-3}, and density ratio $\chi = n_e/n_i = 0.30 \pm 0.16$. These are the averages of 11 oscillating loop events.

2. In a previous study we measured the corresponding oscillation periods, $P = 317 \pm 114$ s, and the damping times, $t_D = 574 \pm 320$ s, which yield a mean ratio of $t_D/P = 1.8 \pm 0.8$. According to the resonant damping

TABLE 4
MEANS AND STANDARD DEVIATIONS OF MEASURED PARAMETERS IN 11 OSCILLATION EVENTS

Parameter	Mean and Standard Deviation
Loop curvature radii $R_{\rm curv}$	57 ± 21 Mm
Oscillation period P	317 ± 114 s
Damping time t_D	574 ± 320 s
Observed number of oscillations t_D/P	1.8 ± 0.8
Predicted minimum of ratio $(t_D/P)_{\rm min}$	0.32 ± 0.05
Outer loop radius a	4.5 ± 3.5 Mm
Inner loop radius $a - l$	0.6 ± 0.5 Mm
Mean loop width $w_{\rm loop} = 2a - l$	5.1 ± 3.9 Mm
Loop skin depth l	3.9 ± 3.1 Mm
Relative loop skin depth l/R	1.5 ± 0.2
Loop density n_i	$(1.4 \pm 0.7) \times 10^9$ cm^{-3}
External plasma density $n_e(T = 1$ MK$)$	$(0.36 \pm 0.18) \times 10^9$ cm^{-3}
Predicted external plasma density $n_e = n_i \chi_{\rm LEDA}$	$(0.76 \pm 0.36) \times 10^9$ cm^{-3}
Density ratio $\chi = n_e(T = 1$ MK$)/n_i$	0.30 ± 0.16
Predicted density ratio $\chi_{\rm LEDA} = n_e/n_i$	0.53 ± 0.12
Prediction ratio $n_e/n_e(T = 1$ MK$) = \chi_{\rm LEDA}/\chi$	2.5 ± 2.1

model of Ruderman & Roberts (2002), originally derived for the thin-boundary approximation and now generalized for the thick-boundary approximation by T. Van Doorsselaere et al. (2003, in preparation), the observed damping times constrain (under the assumption of damping by resonant absorption) a density ratio of $\chi_D = 0.53 \pm 0.12$, which is a factor of $\chi_{\rm LEDA}/\chi \approx 1.2$–$3.5$ higher than that measured from the background fluxes with the *TRACE* 171 Å filter. It is likely that this discrepancy factor results from the neglected hotter plasma with $T \gtrsim 1.5$ MK that is not detected with the 171 Å filter. With this correction, the damping model or resonant absorption can be considered as a successful theory to explain the observed damping times. Alternatively, the model of phase mixing is also found to be consistent with the data.

3. The damping model by resonant absorption provides a direct diagnostic of the density ratio $\chi_D = n_e/n_i$. The observed parameters of the loop cross section profiles vary very little, and the ratio $a/l = 1.18 \pm 0.11$ varies only by $\approx$10% and can be neglected in the damping formula. The correction factor for the thick-boundary treatment can then be taken in the fully nonuniform limit, $q_{\rm TB}(l/R = 2) \approx 1.0$. Therefore, we have a very simple relation that predicts the number of oscillations $N_{\rm osc} = t_d/P$ as a function of the density ratio $\chi_D = n_e/n_i$, or vice versa (eq. [16]),

$$N_{\rm osc} = \frac{t_D}{P} \approx \frac{1}{\pi} \frac{1 + \chi_D}{1 - \chi_D} , \tag{28}$$

$$\chi_D = \frac{n_e}{n_i} \approx \frac{\pi N_{\rm osc} - 1}{\pi N_{\rm osc} + 1} . \tag{29}$$

The relation is plotted in Figure 10 and can be used as an efficient density diagnostic.

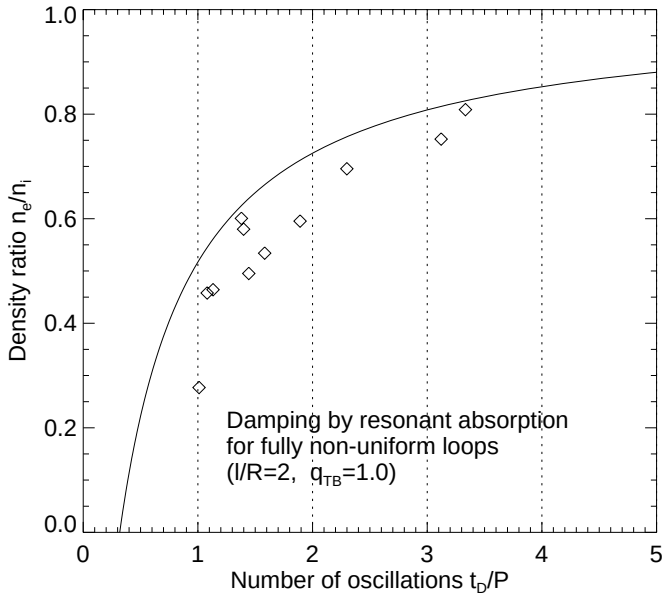

FIG. 10.—Damping mechanism of resonant absorption, which provides a density diagnostic of the density ratio n_e/n_i (of external to internal density in the oscillating loop) as a function of the number of oscillation periods (measured by the ratio of damping time to the period, $N_{\rm osc} = t_D/P$). The plot shows the prediction in the fully nonuniform limit ($l/R = 2$ and $q_{\rm TB} = 1.0$).

This study provides new support for the interpretation of the damping mechanism of coronal loop oscillations in terms of the resonant absorption process. A new effect we learned from this study is the sensitivity to the density contrast between the loop and the ambient plasma. In vacuum, the loop oscillations would be damped within a half oscillation period, $t_D/P \approx 0.5$. However, the higher the ambient plasma density is, the less severe is damping by resonant absorption, so that undamped oscillations can only be supported if the density contrast is very little. Asking the question why only a small subset of all active region loops exhibit oscillations after a global triggering event, e.g., during a flare or a filament destabilization (Schrijver et al. 2002), the mechanism of resonant absorption provides a plausible explanation that oscillations are most favored in loops with little density contrast to the ambient plasma, while all other loops with a large density contrast are strongly damped within a half oscillation period. For future work to study the role of resonant absorption, we recommend to model the differential emission measure distribution of the coronal plasma with multifilter data to obtain a better estimate of the coronal background density.

We thank Bernie Roberts, Valery Nakariakov, Bart DePontieu, and Karel Schrijver for helpful discussions. Part of this work was supported by NASA contract NAS5-38099 (*TRACE*).

APPENDIX

ESTIMATES OF PARAMETER UNCERTAINTIES

The variables of the damping time t_D and period P (Table 1) have been determined in Aschwanden et al. (2002) without an estimate of the uncertainty. Based on multiple trials with different background subtractions, we estimate the uncertainty of the damping time to be of order $\sigma_{t_D} \approx t_D/3$; e.g., compare the result of $t_D = 1200$ s for event 1a in Aschwanden et al. (2002) versus $t_D = 870$ s in Nakariakov et al. (1999). The error in the period measurement P can be neglected because repeated fitting with different background subtractions reproduced this value within a few percent, so the error is much smaller than the error of the damping time t_D. In addition, the errors in the parameters $l_1 - l_0$, $b_1 - b_0$, $R_{\rm curv}$, ϑ and the derived quantities $h_{\rm osc}$ (eq. [25]) and d (eq. [24]) are accurate to a few percent and thus the uncertainties can be neglected. The equivalent column depth $z_{\rm eq}$ (eq. [19]) is a theoretical quantity that has no measurement error.

For all parameters directly measured in this study, $F_{\rm loop}$, $F_{\rm back}$, a, and l (Table 2), we determined the uncertainties $\sigma_{F_{\rm loop}}$, $\sigma_{F_{\rm back}}$, σ_a, and σ_l from the standard deviations that resulted by averaging the fits of all times per event, t_i, $i = 1, \ldots, n$, with typically $n \approx 20$–30 time steps per event.

The uncertainties of the derived parameters n_i (eq. [14]), $q_D = t_D/P$ (eq. [4]), X (eq. [6]), χ_D (eq. [6]), n_0 (eq. [22]), n_e (eq. [23]), and $\chi = n_e/n_i$ (after eq. [1]) were calculated with the error propagation law,

$$\sigma_{n_i} \approx n_i \left(\frac{1}{2F_{\rm loop}} \right) \sigma_{F_{\rm loop}} \ , \tag{A1}$$

$$\sigma_{q_D} = q_D \sqrt{(\sigma_a/a)^2 + (\sigma_l/l)^2} \ , \tag{A2}$$

$$\sigma_X = X \sqrt{(\sigma_{t_D}/t_D)^2 + (\sigma_a/a)^2 + (\sigma_l/l)^2} \ , \tag{A3}$$

$$\sigma_{\chi_D} = \chi_D \left(\frac{2}{X^2 - 1} \right) \sigma_X \ , \tag{A4}$$

$$\sigma_{n_0} = n_0 \left(\frac{1}{2F_{\rm back}} \right) \sigma_{F_{\rm back}} \ , \tag{A5}$$

$$\sigma_{n_e} = n_e \left(\frac{1}{2F_{\rm back}} \right) \sigma_{F_{\rm back}} \ , \tag{A6}$$

$$\sigma_\chi = \chi \sqrt{(\sigma_{n_e}/n_e)^2 + (\sigma_{n_i}/n_i)^2} \ . \tag{A7}$$

REFERENCES

Aschwanden, M. J. 2003, in Turbulence, Waves, and Instabilities in the Solar Plasma, ed. R. von Fay-Siebenburgen et al. (Dordrecht: Kluwer), in press

Aschwanden, M. J., & Acton, L. W. 2001, ApJ, 550, 475

Aschwanden, M. J., DePontieu, B., Schrijver, C. J., & Title, A. M. 2002, Sol. Phys., 206, 99

Aschwanden, M. J., Tarbell, T., Nightingale, R., Schrijver, C. J., Title, A., Kankelborg, C. C., Martens, P. C. H., & Warren, H. P. 2000, ApJ, 535, 1047

Brosius, J. W., Davila, J. M., Thomas, R. J., & Monsignori-Fossi, B. C. 1996, ApJS, 106, 143

Erdélyi, R. 2003, in Turbulence, Waves, and Instabilities in the Solar Plasma, ed. R. von Fay-Siebenburgen et al. (Dordrecht: Kluwer), in press

Golub, L., et al. 1999, Phys. Plasmas, 6, 2205

Goossens, M. 1991, in Advances in Solar System Magnetohydrodynamics, ed. E. R. Priest & A. W. Hood (Cambridge: Cambridge Univ. Press), 137

Goossens, M., Andries, J., & Aschwanden, M. J. 2002, A&A, 394, L39

Goosens, M., Hollweg, J. V., & Sakurai, T. 1992, Sol. Phys., 138, 233

Heyvaerts, J., & Priest, E. R. 1983, A&A, 117, 220

Hollweg, J. V., & Yang, G. 1988, J. Geophys. Res., 93, 5423

Nakariakov, V. M., & Ofman, L. 2001, A&A, 372, L53

Nakariakov, V. M., Ofman, L., DeLuca, E., Roberts, B., & Davila, J. M. 1999, Science, 285, 862

Ofman, L., & Aschwanden, M. J. 2002, ApJ, 576, L153

Poedts, S. 2002, in Proc. SOLMAG: Magnetic Coupling of the Solar Atmosphere Euroconference, ed. H. Sawaya-Lacoste (ESA SP-505; Noordwijk: ESA), 273

Press, W. H., Flannery, B. P., Teukolsky, S. A., & Vetterling, W. T. 1986, Numerical Recipes, The Art of Scientific Computing (Cambridge: Cambridge Univ. Press)

Roberts, B. 2000, Sol. Phys., 193, 139

Roberts, B., Edwin, P. M., & Benz, A. O. 1984, ApJ, 279, 857

Roberts, B., & Nakariakov, V. 2003, in Turbulence, Waves, and Instabilities in the Solar Plasma, ed. R. von Fay-Siebenburgen et al. (Dordrecht: Kluwer), in press

Ruderman, M. S., & Roberts, B. 2002, ApJ, 577, 475

Schrijver, C. J., Aschwanden, M. J., & Title, A. M. 2002, Sol. Phys., 206, 69